Journal of
Astronomical Telescopes,
Instruments, and Systems

AstronomicalTelescopes.SPIEDigitalLibrary.org

Quantum yield estimation for an electron-multiplying charge-coupled device from photon counting test data

Robert Gleisinger
Neil Rowlands
Alan Scott
Olivier Daigle

Robert Gleisinger, Neil Rowlands, Alan Scott, Olivier Daigle, "Quantum yield estimation for an electron-multiplying charge-coupled device from photon counting test data," *J. Astron. Telesc. Instrum. Syst.* **6**(1), 011008 (2020), doi: 10.1117/1.JATIS.6.1.011008

Quantum yield estimation for an electron-multiplying charge-coupled device from photon counting test data

Robert Gleisinger,[a,*] Neil Rowlands,[b] Alan Scott,[b] and Olivier Daigle[c]
[a]University of Victoria, Department of Physics and Astronomy, Victoria,
British Columbia, Canada
[b]Honeywell Aerospace, Ottawa, Ontario, Canada
[c]Nüvü Cameras, Montreal, Québec, Canada

Abstract. Electron-multiplying charge-coupled devices (EMCCDs) allow for subelectron effective read noise and thus for imaging at extremely low flux levels. In the ultraviolet, quantum yield creates an additional source of stochastic gain variation, which can be difficult to quantify using existing techniques. We propose a method for measuring the quantum yield gain of these devices, independent of existing methods, using images that are part of the existing test regimen for new EMCCDs. With this method, we were able to recover the quantum yield used to create simulated images within an accuracy of ~5% and the method provided consistent results with test images after only minor modifications. However, the measured quantum yield remains anomalously low, consistent with other measurements on Teledyne-e2v devices. We hypothesize that this discrepancy is due to lateral transfer of secondary electrons between pixels at the surface explained by the band structure and crystal geometry of typical silicon wafers used in array detector manufacture. [DOI: 10.1117/1.JATIS.6.1.011008]

Keywords: detector arrays; quantum efficiency; ultraviolet.

Paper 19083SS received Aug. 6, 2019; accepted for publication Mar. 2, 2020; published online Mar. 18, 2020.

1 Introduction

NASA's Cosmic Origins Program[1] identifies photon-counting large-format ultraviolet detectors as a top priority technology for future ultraviolet and optical astronomy missions. This technology is seen as a key enabler of both future large aperture space telescopes such as LUVOIR,[2] and moderate aperture survey missions such as CETUS[3] and CASTOR.[4,5] The desired performance requirements are: high quantum efficiency (>70%), large-format (>2k × 2k) detector arrays for operation at 90 to 350 nm wavelength or broader and ideally with red leak (longer wavelength) suppression.[1] Large-area silicon charge-coupled device (CCD) and complementary metal-oxide-semiconductor (CMOS) detectors for near-UV and visible wavelengths are a mature technology. There are numerous optimization processes that can improve the UV detection efficiency of silicon semiconductor material, such as antireflection coatings,[6] chemisorptions treatment,[7] and delta-doping.[8] Due to these factors, much of the technology development effort to address the needs of future UV space astronomy missions is focused on silicon detector arrays. For example, FUV optimized large-format CMOS arrays were evaluated for UV performance in the context of the CASTOR mission. In this case, a CIS113 sensor with Teledyne-e2v's "astro-no-coat" process was procured and tested. Note that the CIS113 was found to have an anomalously low quantum yield.[9] Another aspect on NASA's technology roadmap is photon-counting capability, which is an enabler of future extremely low background visible or UV spectroscopic missions. Currently, these UV photon-counting applications are typically addressed by image intensifiers that do not have high quantum efficiency (typically <15%) and require high-voltage power supplies. Electron-multiplying CCDs (EMCCDs) can deliver photon counting performance in the visible, and since the technologies mentioned above are also applicable to these silicon detector arrays, then UV optimized EMCCDs are a technology of interest. Moreover, recent

---

*Address all correspondence to Robert Gleisinger, E-mail: rgleisinger@uvic.ca characterization results of a $4\text{k} \times 4\text{k}$ EMCCD by Daigle et al.[10] indicate the potential of this technology to also address the need for large-format arrays that can operate at very low fluxes. The combination of large area, photon-counting capability, and UV sensitivity would be unique and an enabler of UV spectroscopic applications. Other applications are also possible, such as space-borne UV auroral imaging, for example, as is planned for the UVI instrument on the SMILE mission[11] currently in development by ESA, the Chinese Academy of Sciences, and the Canadian Space Agency. Use of EMCCD technology in such applications holds the promise of improved imaging resolution and sensitivity over the current image intensifier-based systems. Moreover, large-format arrays potentially enable wide area coverage if red leak issues can be addressed with improved filtering technology. Additional filtering is accomplished by multiple UV reflective mirrors, but including more mirrors to make a silicon-based detector system solar blind becomes problematic for large FOV systems.

An EMCCD takes the usual full-frame CCD architecture and adds an electron-multiplication register between the horizontal "readout" register and the readout electronics. The multiplication register applies a high clock voltage to the CCD output to create additional charges via impact ionization resulting in subelectron effective readout noise levels. EMCCDs are also typically capable of bypassing the electron multiplication register and behaving as a conventional CCD. See Daigle et al.[12] for a discussion of an EMCCD's noise characteristics. Overall, Daigle et al.[12] and Robbins and Hadwen[13] independently found that the effective noise factor $F = \sigma_{\text{out}}/\sigma_{\text{in}}$ of the electron multiplication trends toward $\sqrt{2}$ for high electron multiplication gains, which is a similar effect to halving the quantum efficiency of the CCD in the shot-noise limited signal-to-noise regime. Even with a spurious charge generation rate of 0.06 event/pixel/frame at a flux of 0.2 photon/pixel/frame, Daigle et al.[12] found that the signal-to-noise of the EMCCD is very near the shot-noise limit.

Following on with the promising results obtained with the UV enhanced CIS113 sensor described above, we procured five EMCCD 201-20s from Teledyne-e2v, which were also processed as "astro-no-coat" for enhanced UV sensitivity (in the same manner as the CIS113). Initial UV performance was reported by Rowlands et al.[14] using typical photon transfer methods. Additional UV photon-counting data were also collected and the analysis of these data is reported here. The photon-counting data provide a cross-check of the previous quantum yield measurement results using a new method described in this paper.

2 Quantum Yield

The quantum yield of a detector is the average number of electrons produced by a single-photon hit. When the incident photon energy is greater than the energy gap between the semiconductor valence and conduction band there is a finite probability of more than one electron being generated in the conduction band from a photon absorption. The standard explanation for this is that for sufficient photon energy, the primary photoelectron has some significant probability of ionizing a second atom through impact ionization before it is slowed by electron-phonon interactions. Thus quantum yield >1 is possible in silicon when photon energy exceeds 4.1 eV ($\lambda \sim 300$ nm). This obscures measurements of the interacting quantum efficiency (IQE) of a detector, the probability of a photon hit producing a detected event, by making a single-photon hit appear as two or more events over the integration time. Mathematically, this behaves as a coefficient Q relating the detector's responsive quantum efficiency η_r to its IQE η_i:

$$\eta_r = Q\eta_i. \tag{1}$$

This can be cleared up by an independent measurement of the quantum yield. Unfortunately, all current techniques, including the one described in this paper, depend on multiple variables. The dominant method for this in CCDs is the photon transfer technique described by Janesick,[15] in which the variation in noise level with increasing signal is analyzed to determine the relative contributions of the various sources of noise to the total noise level (note that we have not adopted Janesick's[15] symbol convention). In particular, quantum yield appears in the shot-noise dominated regime that results in a lin-log slope that differs from the ideal $1/2$ dictated by Poisson statistics. This is effective but requires many images with different integration times or different source intensities. Photon transfer analysis is subject to a degeneracy between amplifier Ke gain and quantum yield gain. See Refs. 8 and 16 for examples of photon transfer quantum yield measurement on delta-doped silicon detectors and Ref. 14 for a photon transfer analysis of our device-under-test. It is also possible to establish a lower bound on the quantum yield by measuring the reflectance r of the detector surface and the detector's responsive quantum efficiency. With those, conservation of energy requires that the fraction of photons absorbed cannot exceed $1 - r$ as that would require the detector to absorb some of the photons it is reflecting. In this paper, we refer to this lower bound as the "silicon reflectance" quantum yield estimate.

3 Testing Apparatus and Device-Under-Test

Our device-under-test is a backside-thinned EMCCD 201-20, serial number 15331-11-17, treated with Teledyne-e2v's astro-no-coat process. The device was tested in a liquid nitrogen-cooled camera produced by Nüvü Camēras. The test images were taken by Rowlands et al.[14] as part of their overall tests of the ultraviolet sensitivity of the device and calibrated against measurements of the same illumination source by a National Institute of Standards and Technology (NIST) traceable photodiode (model AXUV100G) and a McPherson ultraviolet scanning monochromator model 234/302 with a 1200 l/mm holographic grating optimized for the near ultraviolet.[14] The test was performed under vacuum in a cryostat, which had been baked out before testing, with a cold plate to account for residual offgassing. For more details on the setup, see block diagram in Fig. 1.[14] Two MgF_2 lenses were used to relay the exit slit of the monochromator to the focal plane located at the EMCCD examples of these images are shown in Fig. 3. Note how the NIST photodiode and its read electronics can be swapped with the test detector for calibration without disturbing the rest of the setup.

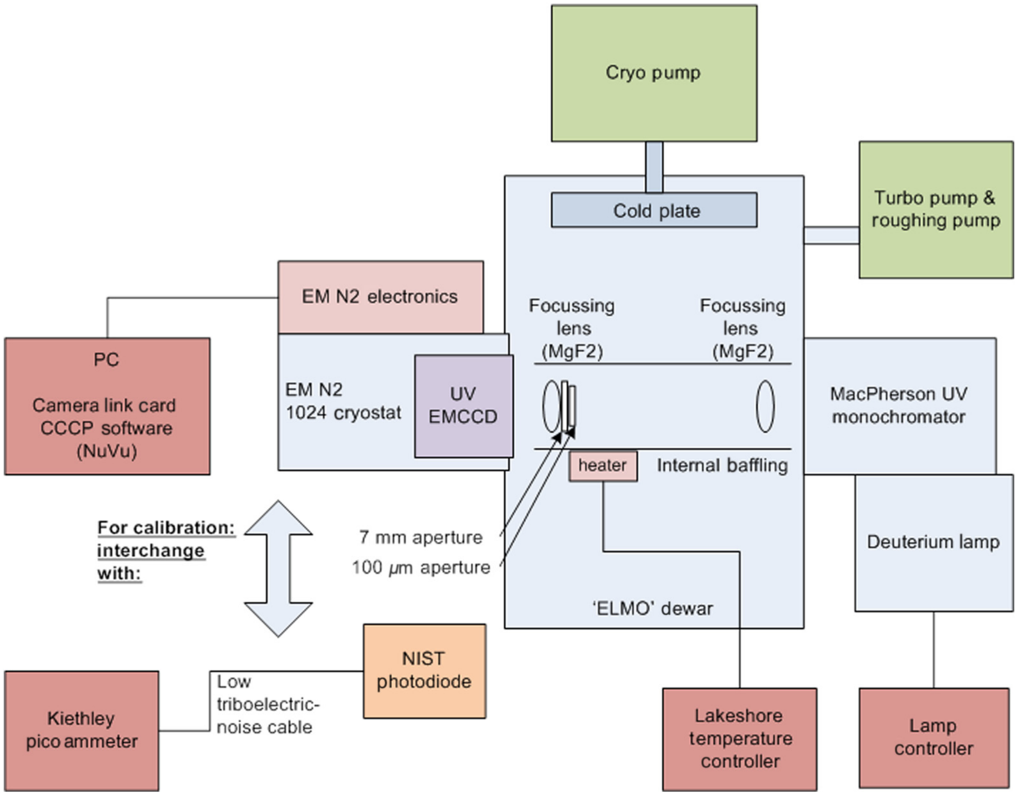

Fig. 1 Block diagram of test apparatus by Rowlands et al.[14] Note the interchangeability between the test assembly containing the device-under-test and the calibration assembly containing the NIST photodiode.

4 Quantum Yield Estimation

4.1 *Photon Counting Method*

The basic concept behind this method is that quantum yield will manifest as an additional source of gain which will apply to illuminated exposures, but not to dark exposures, whereas all other sources of gain will apply equally to both. We do not expect different sources of dark current to affect the results differently because we only need them as a source of signal with no quantum yield gain. Similarly, light with frequency below the threshold for multiple electron generation would work instead of dark signal as it has a known quantum yield of 1 e^-/photon but dark current is likely better as this method relies on the assumption of a low signal level. Mathematically, this means that for quantum yield Q the total gain on the light signal g_L is related to the gain on dark signal g_d by $g_L = g_d \cdot Q$. If we knew g_d and g_L, it would then be trivial to determine Q but in practice this is rarely the case.

The probability p of getting an output x from an EMCCD with input n and mean gain g is given by Daigle et al.[12] as

$$p(x, n, g) = \frac{x^{n-1} e^{-\frac{x}{g}}}{g^n (n-1)!} \tag{2}$$

and the probability P of getting that input n is given by Poisson statistics as

$$P(n, \alpha) = \frac{e^{-\alpha} \alpha^n}{n!}, \tag{3}$$

where α is the mean signal.

Since we do not know the input to the EM register that gave us a certain output, we calculate the probability of getting output x at known mean signal α and mean gain g is a sum over all possible n—the probability of getting that n times the probability of getting x from that n:

$$p_{\text{tot}}(x, g, \alpha) = \sum_{n=1} p(x, n, g) \cdot P(n, \alpha) = e^{-\frac{x}{g}-\alpha} \sum_{n=1} \frac{x^{n-1} \alpha^n}{g^n n! (n-1)!}. \tag{4}$$

For simplicity we only consider $n \leq 2$, which we can do without much loss of accuracy since the mean signal level $\alpha \ll 1$ photons/pixel/frame and each term in the probability decreases according to

$$\frac{p(x, n, g) \cdot P(n, \alpha)}{p(x, n-1, g) \cdot P(n-1, \alpha)} = \frac{x\alpha}{gn(n-1)}. \tag{5}$$

For a test case, similar to Sec. 4.2 of $x = 2000$ and $g \sim 1000$, we find that for a mean signal level of $\alpha \sim 0.10$ photons/pixel/frame (the highest considered in this paper) gives a relative decrease of a factor of $1/30$ between the $n = 2$ term and the $n = 3$ term (a $1/300$ uncertainty on the $n = 1$ first-order approximation), which is small relative to the fitting uncertainties in Secs. 4.2 and 4.3. This approximation leaves us with

$$p_{\text{tot}}(x, g, \alpha) \approx p(x, 1, g) \cdot P(1, \alpha) + p(x, 2, g) \cdot P(2, \alpha). \tag{6}$$

When substituting in Eqs. (2) and (3), we get

$$p_{\text{tot}}(x, g, \alpha) = \alpha e^{-\alpha} \cdot \frac{e^{-\frac{x}{g}}}{g} + \frac{\alpha^2 e^{-\alpha}}{2} \cdot \frac{x e^{-\frac{x}{g}}}{g^2}, \tag{7}$$

we then take the natural logarithm to eliminate the exponentials to get

$$\ln(p_{\text{tot}}) = -\frac{x}{g} + \ln\left(\frac{\alpha e^{-\alpha}}{g}\right) + \ln\left(1 + \frac{\alpha x}{2g}\right). \tag{8}$$

This is where a third-order term would greatly complicate the solution as it results in a quadratic term of $\alpha^2 x^2/12g^2$ (recall that $\alpha \ll 1$ and note that x and g are of the same order of magnitude). Taking the derivative of Eq. (8) with respect to x gives

$$\frac{\mathrm{d}}{\mathrm{d}x}[\ln\, p_{\text{tot}}] = -\frac{1}{g} + \frac{1}{x + \frac{2g}{\alpha}}. \tag{9}$$

These steps represent making a histogram of the image in x and plotting it in lin-(natural) log space and finding the slope to obtain g. This, coupled with the knowledge that x is of the same order of magnitude as g and therefore $\alpha x/2g \ll 1$, is an established technique for estimating the total gain.[17] However, in our analysis of simulated data in Sec. 4.2 we found that level of precision is insufficient; this means that the second term should be retained until the ratio can be simplified with the assumption that $\alpha x/2g \ll 1$. As previously stated, the quantum yield can be obtained by taking the ratio of g_L and g_d, which as shown by Eq. (10) is the same as taking the ratio of the histogram slopes:

$$R = \frac{\text{dark region slope}}{\text{illuminated region slope}} = \frac{\frac{\mathrm{d}}{\mathrm{d}x}[\log_{10} p_{\text{tot,dark}}]}{\frac{\mathrm{d}}{\mathrm{d}x}[\log_{10} p_{\text{tot,light}}]}, \tag{10}$$

and for practical reasons we show that the change of base to $\log_{10}$ has no effect on the ratio

$$R = \frac{\log_{10} e}{\frac{\mathrm{d}}{\mathrm{d}x}[\ln\, p_{\text{tot,light}}]} \cdot \frac{\frac{\mathrm{d}}{\mathrm{d}x}[\ln\, p_{\text{tot,dark}}]}{\log_{10} e} = \frac{\frac{1}{x+\frac{2g_d}{\alpha_d}} - \frac{1}{g_d}}{\frac{1}{x+\frac{2g_L}{\alpha_L}} - \frac{1}{g_L}}, \tag{11}$$

which we simplify to

$$R = \frac{\frac{\alpha_d}{\alpha_d x + 2g_d} - \frac{1}{g_d}}{\frac{\alpha_L}{\alpha_L x + 2g_L} - \frac{1}{g_L}}. \tag{12}$$

We once again assume $\alpha \ll 1$ and $x \sim g$ so that

$$\frac{\alpha}{\alpha x + 2g} \approx \frac{\alpha}{2g}, \tag{13}$$

which gives us a final estimate of the ratio of slopes which we can put in terms of the quantum yield (recall that $g_L = g_d \cdot Q$)

$$R \approx \frac{\frac{\alpha_d}{2g_d} - \frac{1}{g_d}}{\frac{\alpha_L}{2g_L} - \frac{1}{g_L}} = Q\left(\frac{2-\alpha_L}{2-\alpha_d}\right), \tag{14}$$

which we rearrange to get the final estimate for Q in terms of the ratio of slopes R in a lin–log plot of histograms of illuminated and dark regions (dark slope divided by illuminated slope) and the dark and light region signal levels:

$$Q \approx R\left(\frac{2-\alpha_d}{2-\alpha_L}\right). \tag{15}$$

This “correction” based on signal levels assumes known signal levels but is not overly sensitive to errors in signal level. In practice, we determine these signal levels by setting a cutoff of 5σ in each above the offset due to the mean bias for each histogram and integrate (over x) the parts of the histogram above that. Since this is a very conservative estimate we correct the signal levels for the photons that fall below the threshold as described by Daigle et al.[12]; we multiply by $[1-P(x<5\sigma)]^{-1}$ where

$$P(x<5\sigma)=\sum_{x=1}^{5\sigma}\frac{e^{-\frac{x}{g}}}{g} \tag{16}$$

is the Poisson probability that a signal photon will fall below the threshold. As before, x is the output value and g is the total gain. We do not know the total gain with certainty so we take the mean EM gain (1000) for the dark signal correction and the product of the EM gain and slope ratio (as a first-order estimate of QY gain) for the light signal. The Ke gain is already accounted for in the conversion from digital output to electrons. We could also correct for events that were counted as real events but were actually due to read noise, as done by Daigle et al.,[12] by multiplying by $1-0.5[1-\mathrm{erf}(5/\sqrt{2})]=1-2.87\times 10^{-7}$ where erf is the error function. However our high threshold makes this correction negligible. We also subtract our corrected dark signal from our corrected light signal to account for the dark signal in illuminated regions.

4.2 *Demonstration on Simulated Data*

As a demonstration of this method and verification of its effectiveness we use it on simulated test images. All these images have a mean dark signal and clock-induced charge level of 0.002 e^-/pixel. The data set includes sets of images at three signal levels: a set of "darks" for comparison, 0.01 e^-/pixel, and 0.10 e^-/pixel. Each simulated photon has a probability $P_m = Q-1$ of producing two electrons in its pixel rather than just one. Simulated image electrons then undergo a simulated multiplication process with mean EM gain of 1000 output electrons per image electron and Ke gain of unity. Our simulations do not consider the probability of more than one additional quantum yield electron or effects like cross-talk from interpixel capacitance. Note that cross-talk is not expected to have a significant effect at these signal levels.

To start, we take our illuminated frames and we bin all the pixels based on the number of electrons in the pixel and plot this histogram with logarithmic y axis. The resulting plot has a Gaussian-like shape with a linear "tail" at the high-signal end. This linear region is the part whose slope we use to find the quantum yield. We fit a Gaussian to the appropriate part of the domain and a line to the linear part. We then repeat this process for our set of dark frames. We integrate over all bins with a number of electrons more than five times the best-fit standard deviation on the Gaussian component σ in each data set to estimate the signal levels, α_L and α_d, which we correct for the possibility of signal below that threshold using the method we describe in Sec. 4.1 based on a similar method described by Daigle et al.[12] This corrected estimate is ~16% off the simulated input value in the worst case. We then divide the slope of the dark histograms by that of the illuminated histograms, which allows us to find the quantum yield Q with Eq. (15). We show an example histogram from this analysis in Fig. 2 and summarize the results in Table 1.

In an attempt to correct for the fact that there is both dark and light signals in the illuminated images we also ran the analysis again with an extra step in which we subtracted the dark histogram from the light histogram. The idea is that this would leave behind only the light signal. We show both the "uncorrected" and "corrected" results in Table 1. The correction does not impact the results significantly for small values of simulated QY and results in a significant overestimation of the recovered QY at high simulated QY. For the 0.10 e^-/pixel, light levels both the corrected and uncorrected values are overestimated at a QY of 1.25; a more robust method is likely needed for large values of quantum yield at this signal level. We continue to list the "corrected" QY estimates throughout this paper, but we view the uncorrected estimates as more trustworthy. Note that the uncertainties are primarily due to line-fitting uncertainties and Poisson uncertainties $(1/\sqrt{\alpha})$ on the signal levels used in the correction. The line fitting uncertainties are greater for the real test data in Sec. 4.3.

4.3 *Results on Device-Under-Test*

We performed the analysis on 1000 images per wavelength taken with a mean electron multiplication gain of 1000 output electrons per input electron. The illumination was not the same

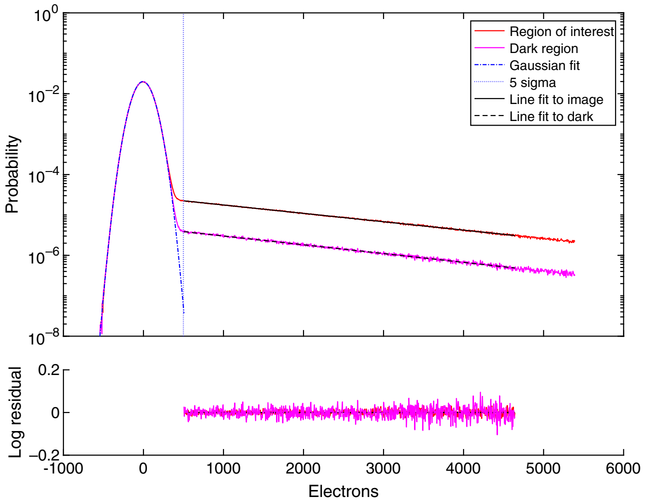

Fig. 2 Example histogram and best-fit lines for quantum yield estimation on simulated data with quantum yield of 1.05 e⁻/photon at a signal level of 0.01 photons/pixel/frame. The upper data series (red) is for the illuminated region and the lower data series (magenta) is for the dark region.

Table 1 Quantum yield results from simulated data. We quote both the "corrected" and "uncorrected" values, but we do not recommend using this correction method because of these results on the simulated data.

Simulated QY (e^-/photon)	Mean signal level (photons/pixel)	Corrected QY (e^-/photon)	Uncorrected QY (e^-/photon)
1.00	0.01	1.002 ± 0.009	1.001 ± 0.009
	0.10	1.000 ± 0.008	0.998 ± 0.008
1.01	0.01	1.013 ± 0.009	1.01 ± 0.01
	0.10	1.008 ± 0.008	1.007 ± 0.008
1.05	0.01	1.05 ± 0.01	1.04 ± 0.01
	0.10	1.052 ± 0.009	1.049 ± 0.009
1.10	0.01	1.11 ± 0.01	1.09 ± 0.01
	0.10	1.111 ± 0.009	1.107 ± 0.009
1.15	0.01	1.17 ± 0.01	1.14 ± 0.01
	0.10	1.17 ± 0.01	1.17 ± 0.01
1.20	0.01	1.24 ± 0.01	1.19 ± 0.01
	0.10	1.24 ± 0.01	1.23 ± 0.01
1.25	0.01	1.31 ± 0.01	1.25 ± 0.01
	0.10	1.32 ± 0.01	1.31 ± 0.01

between wavelengths, at a radiant flux of 3.06×10^4 photon/s at 150 nm, 9.18×10^4 photon/s at 165 nm, and 4.65×10^4 photon/s at 180 nm[14] spread out over an ~60×40 pixel region with exposure times of 1 s. Note that these are a factor of 2.04×10^{-4} lower than those listed by Rowlands et al.[14] due to a 100-μm pinhole placed in front of the 7-mm mask they used for their

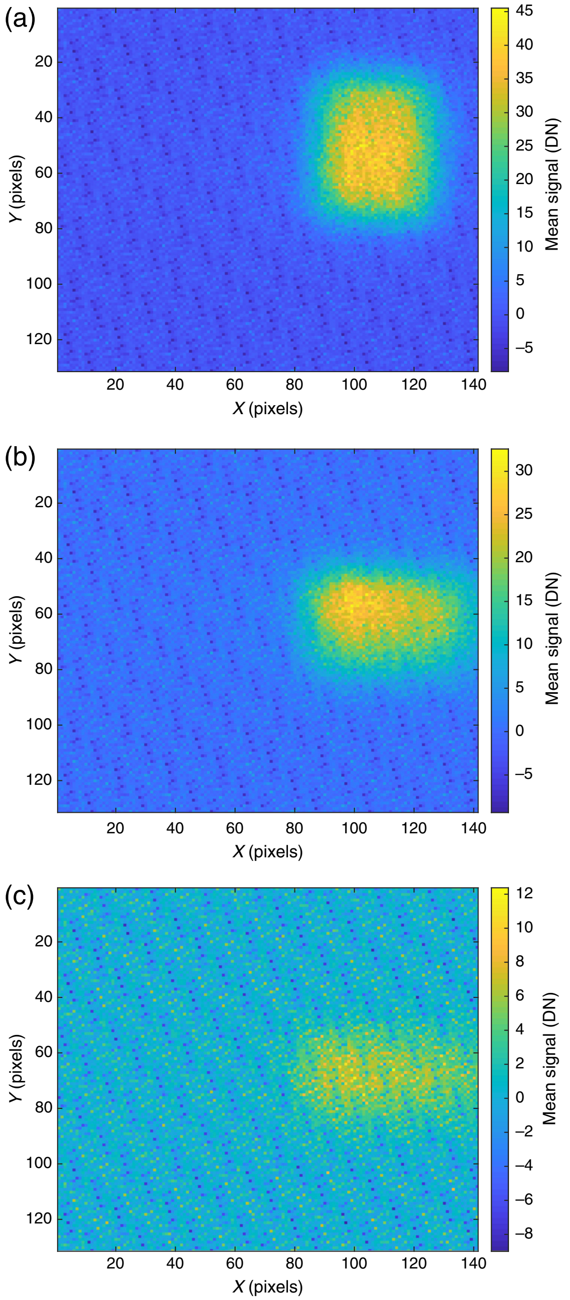

Fig. 3 False color images showing mean illumination of region of interest at each wavelength. Estimated *k*-gain is 23 photon/s. (a) 150 nm, (b) 165 nm, and (c) 180 nm.

quantum efficiency measurements. This means that the illumination level is higher than is ideal for our method. Our dark signal measurements are from an unilluminated region of the same images. We show the mean of all exposures at each wavelength cropped to the region of interest in Fig. 3. Attempts at lower gain levels worked poorly due to the higher input signal levels required to get an image with sufficient signal-to-noise. Attempts at higher gain levels required too much binning to get a smooth curve (empty bins result in the log of zero, i.e., negative infinity). We ended up binning the histograms with increments of five signal levels per bin, but tests with other binning amounts show minimal effect on the output with narrow bin widths. We show the histograms for the real test data in Fig. 4 and summarize the results in Table 2. Our quantum yield measurements are consistently higher than those from the photon transfer method.

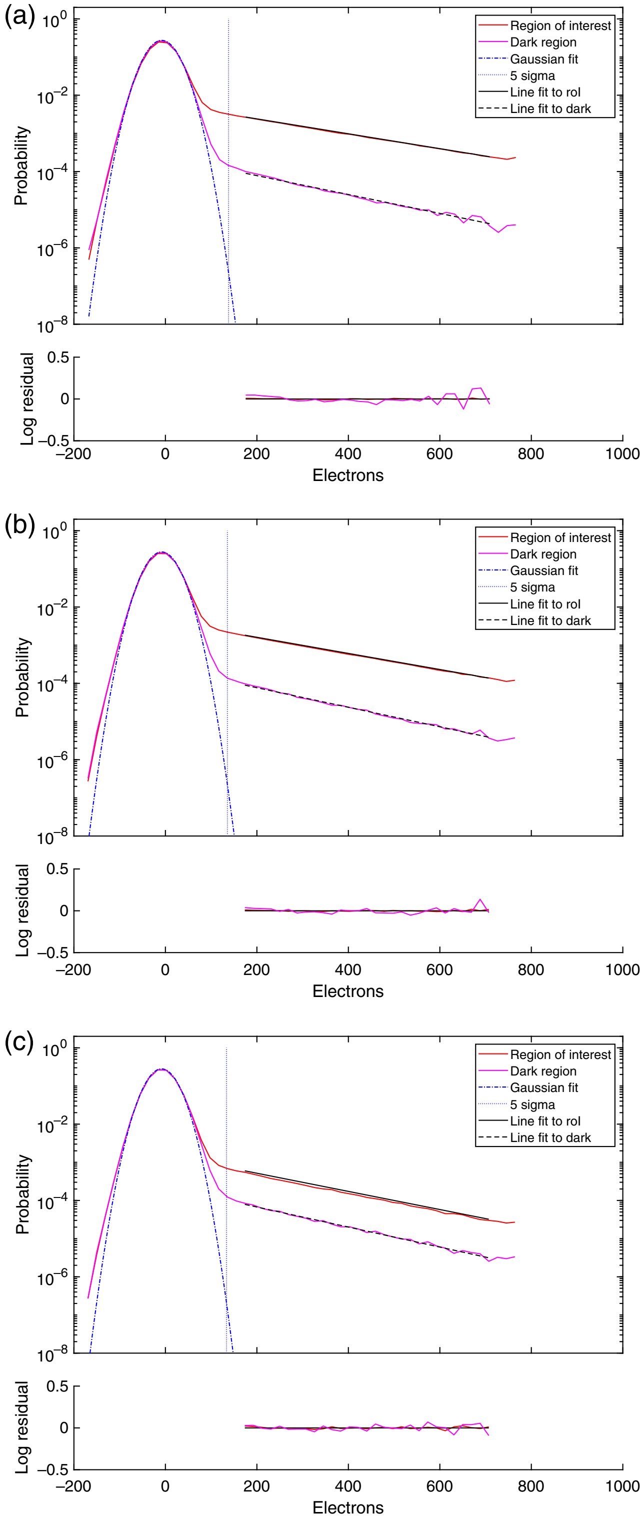

Fig. 4 Quantum yield estimation on test data at electron multiplication gain setting of 1000 output electrons per input electron and estimated *k*-gain of 23 photon/s. The upper data series (red) is for the illuminated region and the lower data series (magenta) is for the dark region. The estimated QY is 1.26 ± 0.08 e$^-$/photon at 150 nm, 1.21 ± 0.05 e$^-$/photon at 165 nm, and 1.12 ± 0.05 e$^-$/photon at 180 nm. (a) 150 nm, (b) 165 nm, and (c) 180 nm.

Table 2 Quantum yield results from device-under-test. Measurements done at EM gain of 1000 output electrons per input electron. QY estimates from photon transfer estimate and silicon reflectance estimate by Rowlands et al.[14] based the silicon reflectance QY estimate on silicon reflectance estimates by Hamden et al.[19]

Wavelength (nm)	Corrected QY estimate (e^-/photon)	Uncorrected QY estimate (e^-/photon)	Photon transfer QY estimate (e^-/photon)	Silicon reflectance QY estimate (e^-/photon)
150	1.27 ± 0.08	1.26 ± 0.08	1.126	1.41
165	1.22 ± 0.05	1.21 ± 0.05	1.037	1.25
180	1.14 ± 0.06	1.12 ± 0.05	1.015	1.07

Table 3 IQE estimates for device-under-test using responsive quantum efficiency (RQE) measurements by Rowlands et al.[14] and quantum yield estimates in Table 2.

Wavelength (nm)	RQE	Corrected IQE estimate	Uncorrected IQE estimate	Photon transfer IQE estimate	Theoretical Si 1-reflectance[19]
150	0.494	0.39 ± 0.02	0.39 ± 0.02	0.439	0.35
165	0.461	0.38 ± 0.02	0.38 ± 0.02	0.445	0.37
180	0.343	0.30 ± 0.02	0.31 ± 0.01	0.338	0.32

Table 4 Quantum yield minimums for uncoated silicon using theoretical data by Hamden et al.[18] (instead of the real measurements by Hamden et al.[19] that we used in Tables 2 and 3) using responsive quantum efficiency measurements for device-under-test by Rowlands et al.[14]

Wavelength (nm)	Theoretical Si 1-reflectance[18]	Theoretical Si reflectance QY estimate
150	0.47	1.05
165	0.42	1.09
180	0.39	1.00

In Table 3, we use the various quantum yield estimates from Table 2 and responsive quantum efficiency measurements by Rowlands et al.[14] to estimate the IQE of the detector. The IQE should not be able to exceed unity minus the reflectance of bare silicon at that wavelength as that would imply that the surface is absorbing photons that should have been reflected at the surface. The photon transfer quantum efficiency estimates are all above the theoretical maximum, and our estimates are consistent with the maximum at 165 and 180 nm but are still elevated at 150 nm. These concerns are eliminated if we use theoretical reflectance estimates by Hamden et al.[18]; however we still propose a possible explanation in Sec. 5.1 for why we might measure quantum yields lower than would be expected from silicon reflectance (Table 4).

5 Discussion

Our method largely retrieved the simulated quantum yield on the simulated data especially at the lower signal level. The quantum yield estimates from both our method and photon transfer are significantly lower than expected from an uncoated silicon interface.[20,21]

Table 5 Quantum yield and quantum efficiency results from CIS113 CMOS detector by Scott et al.[9] Their QY comes from a photon transfer curve fit of $\mathrm{QY} = 2.8 \times 10^{-5}\lambda^2 - 0.016\lambda + 3.38$ based on their own measurements. Their quantum yield estimates are significantly higher than ours despite having the same surface treatment, but their RQE estimates are also significantly higher so their IQE estimates are still greater than the maximum for uncoated silicon.

Wavelength (nm)	RQE (e^-/photon)	Photon transfer QY estimate (e^-/photon)	IQE estimate (e^-/photon)
150	1.08	1.61	0.671
170	0.75	1.47	0.510
180	0.59	1.41	0.418

All QY measurements on this device have been lower than predictions from the reflectance of uncoated silicon at 150 nm. This in itself is not surprising but the QY-adjusted quantum efficiency estimates for the CIS113 at 150 nm are higher than should be possible given the reflectance of bare silicon. We also show similar measurements by Scott et al.[9] on the CIS113 CMOS detector (which has undergone the same Teledyne-e2v astro-no-coat process) for our wavelength range in Table 5 and note how its IQE at 150 nm is greater than it should be for uncoated silicon, though we also note that the different electric field geometries involved in a CMOS architecture may cause significant differences in quantum yield. Similarly, the Hubble Space Telescope's Wide Field Camera 3 is also uncoated silicon and Baggett[22] and Borders et al.[23] found quantum yields up to 30% less than predicted. One possible solution that Rowlands et al.[14] proposed is that the astro-no-coat process does not actively force photogenerated electrons away from the surface so it is more prone to charge trapping and recombination. This is not supported by the measurements of Scott et al.[9] which show that the overall responsivity of the CIS113 CMOS detector is very similar to that measured on a NIST-calibrated uncoated silicon photodiode. However the CIS113 CMOS and CCD201 EMCCD show markedly different responsivity which could potentially be due to such charge trapping in the EMCCD.

5.1 *Lateral Charge Transfer and Quantum Yield*

We hypothesize that the apparent suppression of quantum yield in these detectors is due to lateral charge transfer in cases where secondary electrons are generated. Janesick[15] addressed the possibility and effect of such lateral charge transfer, but we specifically propose a possible mechanism by which such transfer would preferentially affect pixels where secondary quantum yield electrons are generated.

In back-illuminated silicon photodetectors UV photons are absorbed in a relatively field-free region with $1/e$ absorption depths as low as 4 nm. The high-energy conduction band electrons generated here are thus prone to charge trapping in surface defects. Jerram[24] stated that e2v's proprietary astro-no-coat process was developed as an attempt to create a field distribution similar to those created by the NASA Jet Propulsion Laboratory's delta-doping process. Hoenk et al.[25] described delta-doping as using molecular beam epitaxy to implant a layer of negative ions right at the surface to force photoelectrons away from the surface. We show a diagram of the field distribution in an untreated (i.e., not delta-doped) silicon photodetector in Fig. 5; the negative ions introduced by delta-doping reduce the backside potential well and thus reduce trapping near the surface.

The standard model of quantum yield in semiconductor detectors predicts two possibilities for the initial photoelectron; it can lose excess energy through phonon interactions as it travels deeper into the detector medium, or if it has enough energy, it can collisionally excite another valence electron into the conduction band. Since silicon is an indirect bandgap material, excitation transitions below the 3.2 eV direct bandgap are only energetically possible in association with momentum exchange in the [100] crystal direction. In the vacuum UV spectral region primary direct-transition photoelectrons have the potential to scatter off a valence electron to create a second conduction band electron. At the lowest energies this transition can only happen if the valence

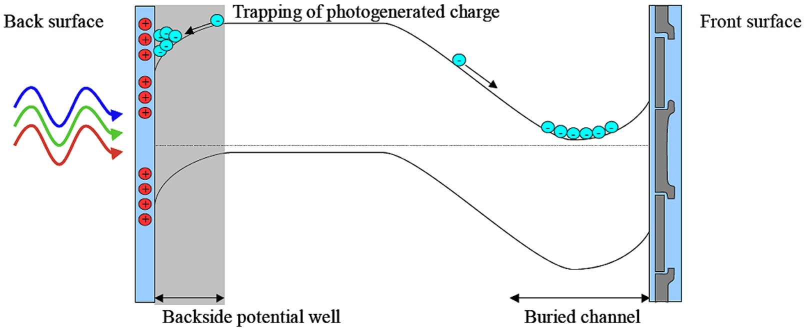

Fig. 5 Electric potential variation with depth in an untreated back-illuminated silicon photodetector.[24]

electron is scattered in the direction of the smallest indirect bandgap. At 4.3 eV (~290 nm) a directly excited photoelectron at the lowest direct bandgap (3.2 eV) would just have sufficient residual energy to excite a secondary photoelectron through the indirect transition. For this to happen the primary photoelectron would have to impart significant momentum in the [100] direction thus taking on opposite momentum in this crystal plane. At higher energies more momentum conserving indirect scattering events become available but in all cases below 6.4 eV (~193 nm where two direct transitions can occur) secondary photoelectrons must be gaining momentum in the [100] plane when they reach the conduction band, requiring opposite recoil momentum to be imparted to the primary. Interestingly, the [100] silicon crystal plane in silicon detectors is parallel to the surface by default of typical wafer geometry such that secondary electrons will preferentially gain momentum in a direction that results in enhanced possibilities for interpixel diffusion. This means that the formation of secondary photoelectrons from high-energy photons results in rapid divergence of the primary and secondary photoelectrons in opposite directions parallel to the detector surface for the most energetically favorable interactions. If these photoelectrons cross pixel boundaries, the quantum yield measured by transfer curve, and single-pixel coincidence methods will appear to be anomalously low.

6 Conclusion

We find that this analysis gives significantly higher quantum yield estimates compared to the existing photon transfer method described by Janesick[15] on the same data set. Our method is independent of the photon transfer method, and therefore is not subject to the same biases. More tests should be done on similar devices to ensure that it generalizes and to further refine the handling of dark signal in the illuminated region. We recommend using a larger illuminated region to improve the statistics without increasing the signal level per pixel per frame. Indeed, the real measurements we present in Sec. 4.3 are analyses of existing data that were at a higher signal level than is ideal for our method.

Interestingly, this method gives quantum yield estimates on the Teledyne-e2v EMCCD 201-20 closer to those Scott et al.[9] found for the Teledyne-e2v CIS113 CMOS detector than those Rowlands et al.[14] found for our device-under-test. Recall that the surface treatment process is the same for the two different devices. However it is possible that variations in the field distribution may impact the fraction of secondary electrons that are captured in a single pixel. We hope to do further point spread function measurements as a function of wavelength to verify this hypothesis. Such measurements may also help confirm our more general hypothesis that the measured QY for the wavelength range (or bandgap energies) considered here are due to photogenerated electrons that are lost to adjacent pixels because here the secondary photoelectrons are preferentially placed in the [100] crystal plane and must move in the opposite direction as the primary photoelectron.

Acknowledgments

We would like to thank Mitacs Accelerate (IT 12685) and the Natural Sciences and Engineering Research Council of Canada's Collaborative Research and Training Experience—New

Technologies for Canadian Observatories for their financial contributions to this project. We would also like to acknowledge the financial support and technical oversight of the Canadian Space Agency under contract No. 9F063/140572/021/MTB to COM DEV Ltd. (doing business as Honeywell Aerospace). The specially processed EMCCDs and original test data were obtained under this project.

References

1. NASA Cosmic Origins Program Office, "Cosmic origins program annual technology report," Tech. Rep. (2012).
2. M. R. Bolcar et al., "The large UV/optical/infrared surveyor (LUVOIR): decadal mission concept design update," *Proc. SPIE* **10398**, 1039809 (2017).
3. S. Heap et al., "The NASA probe-class mission concept, CETUS (cosmic evolution through ultraviolet spectroscopy)," *Proc. SPIE* **10398**, 103980U (2017).
4. P. Côte et al., "CASTOR: the cosmological advanced survey telescope for optical and ultraviolet research," *Proc. SPIE* **8442**, 844215 (2012).
5. P. Côté and A. Scott, "Update on the CASTOR mission concept: scientific opportunities in the Euclid and WFIRST era," *Proc. SPIE* **9144**, 914403 (2014).
6. E. T. Hamden et al., "UV photon-counting CCD detectors that enable the next generation of UV spectroscopy missions: AR coatings that can achieve 80–90% QE," *Proc. SPIE* **8453**, 845309 (2012).
7. M. P. Lesser, "CCD backside coatings optimized for 200- to 300-nm observations," *Proc. SPIE* **4139**, 8–15 (2000).
8. S. Nikzad et al., "Delta-doped electron-multiplied CCD with absolute quantum efficiency over 50% in the near to far ultraviolet range for single photon counting applications," *Appl. Opt.* **51**, 365–369 (2012).
9. A. Scott et al., "NUV performance of e2v large BICMOS array for CASTOR," *Proc. SPIE* **9915**, 99151T (2016).
10. O. Daigle et al., "Preliminary characterization results of a large format 4k × 4k EMCCD," *Proc. SPIE* **10709**, 107090A (2018).
11. W. Raab et al., "SMILE: a joint ESA/CAS mission to investigate the interaction between the solar wind and Earth's magnetosphere," *Proc. SPIE* **9905**, 990502 (2016).
12. O. Daigle, C. Carignan, and S. Blais-Ouellette, "Faint flux performance of an EMCCD," *Proc. SPIE* **6276**, 62761F (2006).
13. M. S. Robbins and B. J. Hadwen, "The noise performance of electron multiplying charge-coupled devices," *IEEE Trans. Electron Devices* **50**, 1227–1232 (2003).
14. N. Rowlands et al., "Ultraviolet sensitivity of a teledyne-e2v EMCCD," *Proc. SPIE* **10709**, 107090D (2018).
15. J. R. Janesick, *Photon Transfer DN → λ*, SPIE Press, Bellingham, Washington DC (2007).
16. B. C. Jacquot et al., "Characterization and absolute QE measurements of delta-doped N-channel and P-channel CCDs," *Proc. SPIE* **7742**, 171–182 (2010).
17. S. M. Tulloch and V. S. Dhillon, "On the use of electron-multiplying CCDs for astronomical spectroscopy," *Mon. Not. R. Astron. Soc.* **411**, 211–225 (2011).
18. E. T. Hamden et al., "Ultraviolet antireflection coatings for use in silicon detector design," *Appl. Opt.* **50**, 4180–4188 (2011).
19. E. T. Hamden et al., "Charge-coupled devices detectors with high quantum efficiency at UV wavelengths," *J. Astron. Telesc. Instrum. Syst.* **2**(3), 036003 (2016).
20. F. J. Wilkinson, A. J. D. Farmer, and J. Geist, "The near ultraviolet quantum yield of silicon," *J. Appl. Phys.* **54**, 1172–1174 (1983).
21. T. Kübarsepp, P. Kärhä, and E. Ikonen, "Interpolation of the spectral responsivity of silicon photodetectors in the near ultraviolet," *Appl. Opt.* **39**, 9–15 (2000).
22. S. Baggett, "WFC3 TV3 testing: quantum yield in the UV," Tech. Rep. (2008).
23. T. Borders, P. McCullough, and S. Baggett, "WFC3 TV3 testing: quantum yield of the UVIS CCDs," Tech. Rep. (2010).

24. P. Jerram, private communication, Teledyne e2v, Chelmsford, England (2014).
25. M. E. Hoenk et al., "Delta-doped back-illuminated CMOS imaging arrays: progress and prospects," *Proc. SPIE* **7419**, 74190T (2009).

Robert Gleisinger is a doctoral student in physics and astronomy at the University of Victoria, in Victoria, British Columbia, Canada. He received his BSc degree in physics from McGill University and his MSc degree in physics and astronomy from the University of Manitoba. His primary research focus is in extragalactic observational astronomy and is currently studying dense star clusters in the Virgo Cluster of galaxies under the guidance of Dr. Patrick Côté.

Neil Rowlands is an engineering fellow at Honeywell Aerospace located in Ottawa, Ontario, Canada. He received his BSc degree engineering physics from the University of Alberta in 1985 and his PhD in astronomy from Cornell University in 1991. Since 1995 he has been developing space-borne scientific instrumentation for the space physics, atmospheric sciences and astronomy communities, including the Canadian contribution to the James Webb Space Telescope (JWST), the Fine Guidance Sensor and Near-Infrared Imager and Slitless Spectrograph (FGS/NIRISS).

Al Scott is an engineering fellow at Honeywell Aerospace located in Ottawa Ontario, Canada. He received his BSc degree in physics from the University of Guelph in 1991 and his PhD in physics from University of Waterloo in 1997. Since then he has been developing optical remote sensing technologies supporting space science and exploration. He is currently the optical architect for Honeywell's optical intersatellite link terminal development.

Olivier Daigle received his BSc degree in electrical engineering from École de Technologie Supérieure in 2001 and graduated in astrophysics from the Univesité de Montréal, during which he studied CCDs and EMCCDs. Following his master's degree in 2005, he was employed in a company that required ultra-sensitive cameras, which inspired him a research project. During his PhD, he developed the technology upon which the company he co-founded in 2010, after graduating from the Université de Montréal, Nüvü Camēras, is built.